ROYAL SOCIETY
OF CHEMISTRY

PAPER

Check for updates

Identifying the roles of acid–base sites in formation pathways of tolualdehydes from acetaldehyde over MgO-based catalysts†

Marcella Lusardi, [iD] [a] Thomas Struble, [iD] [b] Andrew R. Teixeira [iD] [c] and Klavs F. Jensen [iD] *[ab]

Pure and Al-substituted MgO catalysts are studied to identify the contributions of acid–base sites in the formation of two valuable xylene analogs, *ortho*- and *para*-tolualdehydes, from an ethanol derivative, acetaldehyde. The catalyst properties are characterized through XRD, ^{27}Al MAS NMR, ICP-AES, N_2 physisorption, TPD-MS, and DRIFTS experiments. Reactivity comparisons of untreated and CO_2-titrated catalysts at 250 °C, coupled with CO_2 DRIFTS studies on fresh and spent samples, indicate the formation of tolualdehydes from intermediates is initiated through deprotonation by a medium-strength basic site in a specific, metal–oxygen (M–O)-type coordination environment. Analyses of the catalytic surface properties and reactivity, pathways of formation, and natural bond orbital (NBO) charge distribution suggest $C_4 + C_4$ (rather than $C_2 + C_6$) mechanistic steps dominate tolualdehyde production over these catalysts under the investigated reaction conditions. Isomeric selectivity to *ortho*-tolualdehyde is 92 and 81 mol% over pure and Al-substituted MgO catalysts, respectively. We propose that the shift in isomeric selectivity towards *para*- upon introduction of a proximal Lewis acidic functionality (Al^{3+}/MgO) to the catalyst is caused by electron redistribution in the conjugated enolate from the γ-C (forming *ortho*-) towards the α-C (forming *para*-) due to the carbonyl-O/Lewis acid coordination. This insight provides a framework for the development of next generation catalysts that give improved reactivity in cascade reactions of C_2 feedstocks to aromatics.

1 Introduction

The plastics, textiles, solvents, and composite materials derived from BTX (benzene, toluene, and xylenes) are fundamental to many industries.[1] As a result, global demand for these aromatic platform chemicals is high ($\sim$85 MT y^{-1})[1–4] and is expected to increase 5–10% over the next decade as existing industries grow and international economies develop.[5–8] Currently, catalytic reforming of petroleum naphtha produces approximately 70% of BTX.[8] The volatility of petroleum markets, coupled with environmental impacts of petroleum consumption, motivate the diversification of sources for BTX and other valuable petroleum derivatives.[3,4,9] A major challenge in obtaining drop-in chemicals from alternative feeds (*e.g.*, biomass) is the development of new

process pathways and catalysts, given their distinct chemical makeup (oxygen content, molecular weight, *etc.*) compared to that of petroleum.

A bottom-up approach involving the construction of aromatic rings from smaller molecules is one potential route, which could find utility for low-molecular weight, oxygenated feedstocks produced from renewably-sourced biomass or syngas conversion technologies.[8,10,11] Ethanol is one such feed that could be upgraded through a complex series of reactions *via* its dehydrogenated intermediate, acetaldehyde.[12,13] Aromatic compounds (benzene, tolualdehydes) can be produced through several different mechanisms (aldol condensation, Michael addition, dehydration, electrocyclization, *etc.*) involving acetaldehyde and its condensation products (Scheme 1).[11,12,14,15] While the benzene mechanism is straightforward,[14] the formation of tolualdehydes, which are valuable xylene analogs (Scheme S1†), is more complicated. To date, work on this reaction has focused predominantly on understanding the mechanistic routes and kinetics associated with the complex pathways.[11,16,17] Moteki *et al.* identified the different pathways that can yield two isomers of tolualdehyde, *ortho*- and *para*-, from ethanol, acetaldehyde, and intermediates

[a] Materials Science and Engineering, Massachusetts Institute of Technology, Cambridge, MA, 02139 USA
[b] Chemical Engineering, Massachusetts Institute of Technology, Cambridge, MA, 02139 USA
[c] Chemical Engineering, Worcester Polytechnic Institute, Worcester, MA, 01609 USA. E-mail: kfjensen@mit.edu
† Electronic supplementary information (ESI) available. See DOI: 10.1039/c9cy01927h

This journal is © The Royal Society of Chemistry 2020
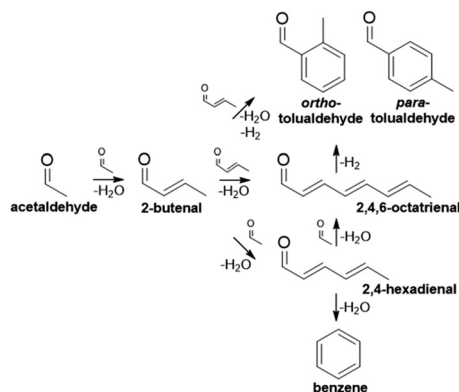
Scheme 1 Overview of cascade reaction pathways that produce aromatics (benzene, tolualdehydes) from acetaldehyde.

over hydroxyapatite catalysts.[12] Zhang and co-workers investigated these routes as well by directly feeding the acetaldehyde dimer, 2-butenal, over MgO- and ZrO$_2$-incorporated faujasite.[18] They proposed a likely route of *ortho*- and *para*-tolualdehyde formation based on their experimental yields and a more-energetically favorable enolate intermediate calculated through DFT analysis. Recent work[17] investigated the use of a dual-bed Cu/C and Co-hydroxyapatite system to catalyze ethanol dehydrogenation to acetaldehyde followed by coupling to aromatic aldehydes and alcohols, and the associated rates of each step.

As mechanistic and kinetic understanding of these tolualdehyde formation routes has increased, the nature of the active sites for obtaining tolualdehydes from intermediates remains largely unexplored. Prior investigations[19–23] have identified the active sites for the formation of C$_4$ intermediates (butenal—the first step in the cascade reaction) and products (butanol, butadiene) from C$_2$ compounds over a range of different catalysts. Recently, the active coordination environment for the formation of C$_{6+}$ products from ethanol over hydroxyapatite was identified.[24] These products were strictly aliphatic and formed through a direct ethanol coupling mechanism, not *via* an acetaldehyde intermediate that can form tolualdehydes. To the best of our knowledge, no work has studied the specific nature of the active basic site(s) responsible for initiating the tolualdehyde formation mechanism *via* proton abstraction from intermediates. Thus, the primary focus and contribution of this work is the characterization of active sites in the second step of the cascade reaction to form C$_8$ aromatics as the terminal products through C$_2$ + C$_6$ cross-condensation and/or C$_4$ + C$_4$ self-condensation routes. In parallel, we determine the more likely of those two routes for the catalysts and reaction conditions used in this study.

MgO-based catalysts were chosen as the candidates to study the nature of the active site(s) in this reaction. MgO-based catalysts exhibit the high basic character necessary to promote condensation pathways over other potential acetaldehyde routes (*e.g.*, coking and cracking, reductive coupling)[25–29] and have shown multiple condensation activity (*i.e.*, condensations

that yield trimers, tetramers, *etc.*) in previous studies.[15,18,30–32] Different coordination environments on MgO surfaces give rise to a wide distribution of basic site types and strengths, which enables the screening of such sites for their contribution to the formation of aromatic products from C$_2$ feeds.[33] To probe the impact of acidity, which can contribute in aldol condensation-type mechanisms through acid–base cooperation,[30,34–38] varying amounts of Al^{3+} were introduced into the MgO lattice. Partial isomorphic substitution of Al^{3+} for Mg^{2+} in the octahedral sites of the face-centered cubic lattice generates Lewis acidity through Al^{3+} cations exposed on the surface.[39] In addition to introducing an acidic functionality, Al incorporation can affect the basic properties of the mixed oxide by creating both relatively weaker and very strong basic centers in the mixed oxide compared to that of the pure periclase (MgO) phase.[19,40,41] Thus, varying the amount of Al incorporated can have a significant impact on the acid–base character of the Mg–Al oxide.

To understand the impact of the surface chemistry on the formation of aromatics from an ethanol derivative, with the overall goal of identifying the nature of the active basic site(s) and potential contributions from catalyst acidity, we prepared catalysts with various degrees of Al content (molar Al/(Mg + Al) = 0, 0.25, and 0.33). In particular, we studied the formation of *ortho*- and *para*-tolualdehydes from acetaldehyde over these catalysts, and analyzed the catalytic reactivities in the contexts of their surface properties and possible mechanistic routes. From these studies, we characterize the roles of different site types and propose likely pathways of tolualdehydes formation over the MgO-based catalysts studied here. The insight obtained from these studies is critical to direct next generation catalyst design for improved reactivity in the formation of valuable aromatics from C$_2$ feedstocks.

2 Materials and methods

2.1 Catalyst synthesis

2.1.1 Al-substituted MgOs. Al incorporation into the MgO framework was achieved through the calcination of Mg–Al layered double hydroxide (LDH) precursors. LDHs with different Al contents (molar Mg/Al = 2 and 3) were synthesized using a typical co-precipitation technique at a constant pH of 10. Details of the synthesis are outlined in the ESI.† The Al-substituted MgOs were obtained through calcination of the LDHs at a 10 °C min^{-1} ramp and an 8 h soak at 550 °C in static air. These calcined samples are referred to as Mg$_x$Al-ox, where x is the nominal molar Mg/Al.

2.1.2 Pure oxides. Pure hydroxides were prepared using similar co-precipitation synthesis parameters. The obtained Mg(OH)$_2$ precipitate was calcined using the same program as the LDHs to yield MgO. A milder calcination program (10 °C min^{-1} ramp to 450 °C, 8 h soak, static air) was used to obtain γ-Al$_2$O$_3$ from Al(OH)$_3$ for the mechanical mixture experiments.

2.2 Catalyst characterization

2.2.1 Physicochemical characterization. Powder X-ray diffraction (XRD) experiments were conducted on the as-synthesized hydroxide and oxide samples for phase analysis. XRD measurements were taken on a PANalytical X'Pert Pro instrument using Cu Kα radiation (λ = 1.54184 Å). A Rietveld refinement on the diffraction data was conducted using PANalytical X'Pert HighScore Plus software v3.0 by varying the scale factor, unit cell, specimen displacement, and the Cagliotti w parameter to minimize the difference curve to determine the phase distribution in the mixed oxide (Mg_xAl-ox) catalysts. Inductively coupled plasma atomic emission spectroscopy (ICP-AES) measurements were taken on an Agilent 5100 Dual View unit in radial view at a viewing height of 8 mm to determine the actual Mg/Al in the Mg_xAl-ox samples. Calibration samples were prepared from a commercial standard (Inorganic Ventures, Cool Plasma ICP-MS Complete Standard). Survey X-ray photoelectron spectra were collected on a PHI Versaprobe II XPS. [27]Al magic angle spinning nuclear magnetic resonance (MAS NMR) spectroscopy was used to analyze the local Al coordination environments in the Mg_xAl-ox catalysts. These experiments were run on a Varian Inova 500 spectrometer using a 3 mm rotor spun at 12 kHz. Textural properties were investigated using a QuantaChrome AutoSorb iQ instrument to collect liquid N_2 adsorption–desorption isotherms (77 K). Prior to analysis, samples were outgassed at 250 °C for 6 h to clean and dry the surface.

2.2.2 Surface chemistry characterization. The acid–base properties of the pure and Al-substituted MgO catalysts were quantified through probe molecule temperature programmed-desorption-mass spectrometry (TPD-MS) studies using a microreactor system built in-house. In a typical experiment, 20 mg of oxide catalyst (sized between 75 and 125 μm) was packed onto a bed of quartz wool. The sample was heated in a flow of 1% Ar/99% He at 450 °C for 1 h to remove surface adsorbates, cooled down to 50 °C, and saturated with the acid (CO_2) or base (NH_3) probe molecule (1%/99% He) at that temperature. After reaching the probe molecule baseline value, the catalyst was subjected to a 5 °C min^{-1} ramp in a flow of 1% Ar/99% He. The evolution of CO_2 or NH_3 was quantified using a calibrated MS (Inificon Transpector 2) signal and Ar as the internal standard. Blanks were run on a bed of quartz wool and these integrated values were subtracted from the reported site densities.

Diffuse reflectance Fourier transform infrared spectroscopy (DRIFTS) experiments were run to further characterize the nature of the basic sites present on the oxide catalysts using CO_2 as a probe molecule.[42] DRIFTS measurements were taken on a Bruker Vortex 70 benchtop FTIR equipped with a Harrick Praying Mantis diffuse reflectance cell and a liquid N_2-cooled mercury-cadmium-telluride (MCT) detector. Atmosphere and temperature control were achieved with a high-temperature chamber built with ZnSe windows. DRIFTS samples were prepared by diluting the catalyst to 20 wt% with KBr. After pretreatment in He at 450 °C for 1 h, the sample was cooled to 50 °C in 50

°C increments, and a reference sample was collected at each temperature. The sample was then saturated at 50 °C with the probe molecule (10% CO_2, 90% N_2) and flushed with He to remove physisorbed species. Subsequently, a sample was collected after 15 min evacuation at each temperature to evaluate the CO_2 interaction with the oxide surface. The results are plotted in Kubelka Munk ($f(R_\infty)$) units at each temperature, where R_∞ is the CO_2-saturated sample referenced to the cleaned sample at the same temperature.[43] CO_2 DRIFTS analysis using the same procedure was also conducted on spent MgO after a given time on steam.

2.3 Catalytic reactivity

The activity of the catalysts was evaluated in a vapor phase flow system at ambient pressure. 10 mg of catalyst sized between 75 and 125 μm was packed onto a bed of stainless steel beads in a 2.5″ L × 0.049″ ID micro packed bed reactor. After *in situ* pretreatment of the catalyst in 10 sccm of N_2 for 0.5 h at 350 °C, the acetaldehyde vapor (0.1%/99.9% N_2, Airgas) was introduced at 10 sccm, which corresponds to a ~10 ms residence time. The reactor temperature was 250 °C in all runs. Transfer lines downstream of the reactor were heated to prevent condensation of heavier intermediates and products. Samples were analyzed with an Agilent G1888 head space sampler retrofitted for online gas-phase analysis and an Agilent 7890A gas chromatograph (GC) equipped with a flame ionization detector (FID) for species quantification. The carbon balance for all reactions (inclusive of carbonaceous deposits quantification by oxidative thermogravimetric analysis, TGA) was >90%. Yields are reported on a mole carbon basis. Experiments were duplicated and the variation between the two runs is shown by error bars. For the mechanical mixture test, we gently mixed together weights of MgO and γ-Al_2O_3 that gave 10 mg total oxide with a molar Mg/Al = 2.

In situ CO_2 titration studies were conducted to distinguish the activity contribution by strong basic sites (*i.e.*, sites whose temperature of CO_2 desorption is higher than the reaction temperature of 250 °C). In these experiments, the catalyst was subjected to an additional pretreatment step. After cleaning and drying the catalyst at 350 °C in N_2, the packed bed was cooled to 50 °C, and a 10 sccm flowrate of 10% CO_2/90% N_2 was introduced to saturate the catalyst surface. Subsequently, the bed temperature was increased to the reaction temperature (250 °C) in the diluted CO_2 mixture. The reaction proceeded as outlined above, except that CO_2 was co-fed with the 0.1% acetaldehyde vapor (0.1% acetaldehyde/10% CO_2/89.9% N_2, Airgas).

2.4 Computational methods

DFT calculations were performed using Gaussian 16 (ref. 44) in order to carry out the NBO analysis (NBO version 3.1 (ref. 45)). Geometry optimizations were done using the B3LYP[46]/6-311+g(d,p) functional. All optimized structures were verified by frequency computations as minima (zero imaginary frequencies).

538 | *Catal. Sci. Technol.*, 2020, **10**, 536–548

This journal is © The Royal Society of Chemistry 2020

3 Results and discussion

3.1 Catalyst characterization

3.1.1 Physicochemical characterization.
XRD analysis of the synthesized materials show LDH (Mg$_x$Al-LDH) and hydroxide (Mg(OH)$_2$) phases (Fig. S1a and b,† respectively). Upon calcination, all catalysts show a periclase (MgO) phase (Fig. 1). The phase distributions calculated from the Rietveld refinement on the XRD data (Fig. S2a†) show that, despite some spinel-like (MgAl$_2$O$_4$) content, periclase is the primary phase in the Mg$_x$Al-ox. Thus, the catalysis on these samples is likely dominated by its most stable plane of cleavage, {100}.[47] The shifts to larger 2θ values of the (200) diffraction peaks for the Mg$_x$Al-ox confirm that there is modification of their periclase phases, and thus the acid–base properties of their surfaces, through isomorphic Al incorporation: the lattice parameter a (Table 1) linearly contracts (Fig. S2b†) with increasing Al content due to the smaller radius of Al (0.535 Å) compared to Mg (0.720 Å).[48–50]

^{27}Al MAS NMR spectra (Fig. S3†) show two resonances corresponding to two major Al coordination environments: octahedral (Al$_O$, 10–14 ppm) and tetrahedral (Al$_T$, 72 ppm). The absence of peak splitting to reflect the presence of octahedral and tetrahedral Al^{3+} in periclase and spinel-type phases indicates that the Mg$_x$Al-ox samples are more disordered in nature. Thus, a wide distribution of coordination environments and corresponding acid–base sites is possible. ICP-AES results summarized in Table 1 show that the actual Mg/Al values obtained are in good agreement with the expected values based on the initial metal salts concentrations prepared during the co-precipitation syntheses. No residual Na content from the syntheses was detected by ICP or XPS (Fig. S4†).

From the N$_2$ adsorption–desorption measurements at 77 K, we report BET surface areas and total pore volumes in Table 1. The raw isotherms for the Mg$_x$Al-ox and MgO catalysts are presented in Fig. S5.† The smallest pore diameters (pore size distributions, Fig. S6†) measured in Mg$_x$-Al-ox and MgO are much larger (>2×) than the pores that give rise to aromatics shape and/or size selectivity due to confinement (e.g., ZSM-5 with d_{pore} ~ 6 Å).[51] Thus, differences in isomeric selectivity amongst these catalysts can be attributed to variations in surface chemistry, rather than to pore confinement effects.

3.1.2 Surface chemistry characterization.
The CO$_2$ and NH$_3$ TPD-MS profiles for Mg$_x$Al-ox and MgO are shown in Fig. 2a and b, respectively, and integrated basic and acid site densities are reported in Table 1. A detailed discussion of the TPD results is contained in the ESI.† Briefly, the oxide catalysts exhibit CO$_2$ desorption peaks across a range of temperatures from 100 to 700 °C, indicating the presence of weak, medium-strength, and strong basic sites, corresponding to differential heats of CO$_2$ adsorption of 70–120 kJ mol^{-1}, 120–150 kJ mol^{-1}, and >150 kJ mol^{-1}, respectively.[52] The basic site density decreases with increasing Al content, while the acid site density increases with increasing Al incorporation. The comparable profile shapes for the Mg$_x$Al-ox demonstrate similar acid site types across these samples, and previous work has reported these sites to be of Lewis type with intermediate strength (differential heats of NH$_3$ adsorption ranging from 70–130 kJ mol^{-1}).[39,53] On the other hand, pure MgO exhibits a very low acid site density (0.07 μmol m^{-2}), which suggests that Mg^{2+} cations on {100} surfaces do not contribute appreciably to catalyst acidity. This is consistent with previous reports that MgO has very weak acid character both in site density and strength (differential heat of NH$_3$ adsorption ≈ 55 kJ mol^{-1}).[33,39]

CO$_2$ DRIFTS studies were run to further understand the nature of basic sites present on the Mg$_x$Al-ox and MgO catalysts. CO$_2$ DRIFTS profiles in the full temperature range (50 to 350 °C) are reported in Fig. S7† and a comparison of profiles for Mg$_x$Al-ox and MgO at 50 °C and 200 °C is shown in Fig. 3a and b, respectively. Given the difficulty of linearizing DRIFTS signals with adsorbate concentrations,[43,54] the analysis here is limited to strictly qualitative comparisons.

The spectra for all samples (Fig. 3a) show features attributed to bicarbonate, bidentate, and monodentate structures, which correspond to CO$_2$ adsorption on weak hydroxyl groups, medium-strength metal–oxygen (M–O) pairs, and strong low-coordinated oxygen sites, respectively.[19,33,39] The Mg$_x$Al-ox spectra exhibit quite similar features, indicative of similar basic site coordination environments on these Al-substituted samples regardless of Al content (25 and 33 mol% Al). Over Mg$_x$Al-ox, a strong peak appears around 1660–1700 cm^{-1} which corresponds to the asymmetric stretching mode of O–C–O–H in the bicarbonate structure.[19,42,55] The symmetric stretching mode appears as an indistinct feature around 1450 cm^{-1}.[19,40] The C–OH bending vibration, δ(C–OH), appears clearly at 1220 cm^{-1} for the Mg$_x$Al-ox samples.[19,40,42] In the MgO spectrum (Fig. 3a), the asymmetric stretching mode of the bicarbonate manifests from 1660–1710 cm^{-1}. The symmetric stretching and bending modes for bicarbonate over MgO appear at 1460–1470 and 1235 cm^{-1}, respectively.

Bidentate carbonate features in the Mg$_x$Al-ox spectra appear at 1590–1650 cm^{-1} for the v(C═O) mode; and at 1315–1330 cm^{-1} and ~1075 cm^{-1} for the v(O–C–O) asymmetric and symmetric stretching modes,

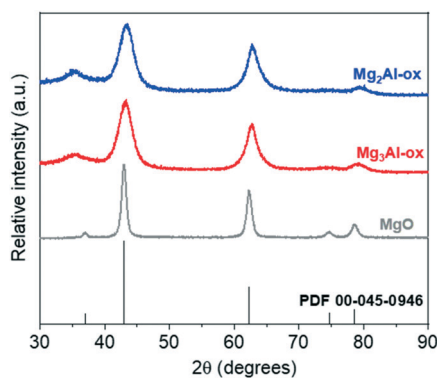**Fig. 1** XRD patterns for Mg$_x$Al-ox and MgO, and the reference pattern for periclase.

Table 1 Summary of physicochemical and surface chemistry properties for the Mg_xAl-ox and MgO samples

Sample	Lattice parameter a^a (Å)	Mg/Al^b (mol/mol)	BET surface area^c ($m^2\ g^{-1}$)	Total pore volume^c ($cm^3\ g^{-1}$)	$n_B{}^d$ ($\mu mol\ m^{-2}$)	$n_A{}^d$ ($\mu mol\ m^{-2}$)
Mg_2Al-ox	4.155	2.07	249	0.783	1.25	1.46
Mg_3Al-ox	4.172	3.09	268	0.598	1.36	0.87
MgO	4.208	—	140	0.318	2.59	0.07

^{a} Calculated from (200) diffraction. ^{b} Measured by ICP-AES. ^{c} Calculated from N_2 adsorption–desorption isotherms (77 K). ^{d} Measured by CO_2 (n_B) and NH_3 (n_A) TPD-MS.

respectively.[19,42,55,56] For MgO, bidentate modes present as distinct peaks at 1600–1650 cm^{-1}, a shoulder at 1310–1350 cm^{-1}, and a broad feature at 1085 cm^{-1}. Fig. 3b shows the spectra taken at 200 °C for Mg_xAl-ox and MgO. At this temperature, bicarbonate structures are no longer present; and bidentate structures, which correspond to CO_2 adsorbed on medium-strength M–O pairs, are stable on MgO materials and disappear by 300 °C.[33] Two bidentate $\nu(C{=}O)$ modes appear at frequencies ≥1600 cm^{-1} over MgO. While these modes exhibit comparable temperature stabilities (disappear by 250 °C), the difference in their frequency values (45 cm^{-1}) suggests different site strengths and/or local geometries due to varied M–O coordination environments, both of which can impact catalytic activity.[57–59] The breadth of the Mg_xAl-ox spectra prevents distinguishing different bidentate structures corresponding to varied M–O coordination types that might be present, but a shoulder is visible at 1620–1650 cm^{-1} that corresponds to at least one $\nu(C{=}O)$ mode on the Al-substituted samples (Fig. 3b).

Lastly, these materials exhibit features attributed to monodentate carbonates, which form from adsorption of CO_2 on low-coordinated O^{2-} proximal to defects and are stable at high temperature (≥300 °C).[33,55] The asymmetric and symmetric $\nu(O–C–O)$ modes for the Mg_xAl-ox appear at 1500–1575 cm^{-1} and 1335–1425 cm^{-1}, respectively; a broad feature corresponding to $\nu(C–O)$ weakly presents at ~1030 cm^{-1} (Fig. 3a).[19,33,42,55,60] Over MgO, the asymmetric and symmetric $\nu(O–C–O)$ modes appear in the ranges 1495–1545 cm^{-1} and 1385–1440 cm^{-1}, respectively, while the $\nu(C–O)$ appears below 1000 cm^{-1}. At higher temperature (Fig. 3b), a more complex spectrum manifests quite distinct site types corresponding to carbonate formation on medium-strength and strong basic sites. Some of these features for MgO (e.g., the sharp peak at 1330 cm^{-1}) have frequencies outside the expected range for monodenate modes. Given their

persistence at high temperature (350 °C), and the magnitude of the split, $\Delta \nu_3$, between symmetric and asymmetric modes, we assign them to polydentate structures attributed to a strong, basic O^{2-} center.[61,62]

As a general conclusion, the CO_2 DRIFTS studies show that varying the amount of Al incorporated (in the range of molar Mg/Al = 2 and 3) does not significantly impact the nature or type of basic sites present, while CO_2 TPD-MS experiments illustrate that Al content does affect total basic site density and the densities of various site types (e.g., lower temperature peak maximum for Mg_3Al-ox is shifted +100 °C relative to maximum for Mg_2Al-ox). In the absence of isomorphic Al substitution (i.e., pure MgO), the resulting oxide has a narrower distribution of sites and the strongest basic character.

3.2 Aromatics production from acetaldehyde over Mg_xAl-ox and MgO catalysts

Acetaldehyde and its products can undergo a complex reaction network (Scheme 1) to yield the target aromatic species. The yields for the products 2-butenal, benzene, and tolualdehydes are reported in Fig. 4(a)–(c). Conversion and full product distributions are plotted in Fig. S8 and S9,† respectively. Given the extremely low yields of benzene, this discussion will focus on the other aromatic product of interest, tolualdehydes. The benzene results are summarized in the ESI† (Fig. S10 and Scheme S2).
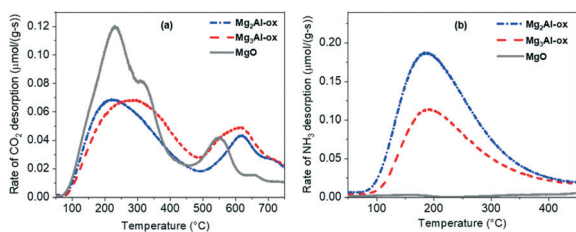

Fig. 2 (a) CO_2 and (b) NH_3 TPD-MS profiles for Mg_xAl-ox and MgO for basic and acid site quantification, respectively.
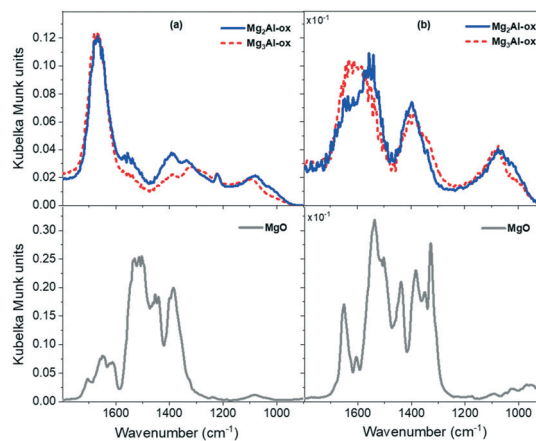

Fig. 3 DRIFTS spectra of CO_2 adsorbed on Mg_xAl-ox and MgO at (a) 50 °C and (b) 200 °C.
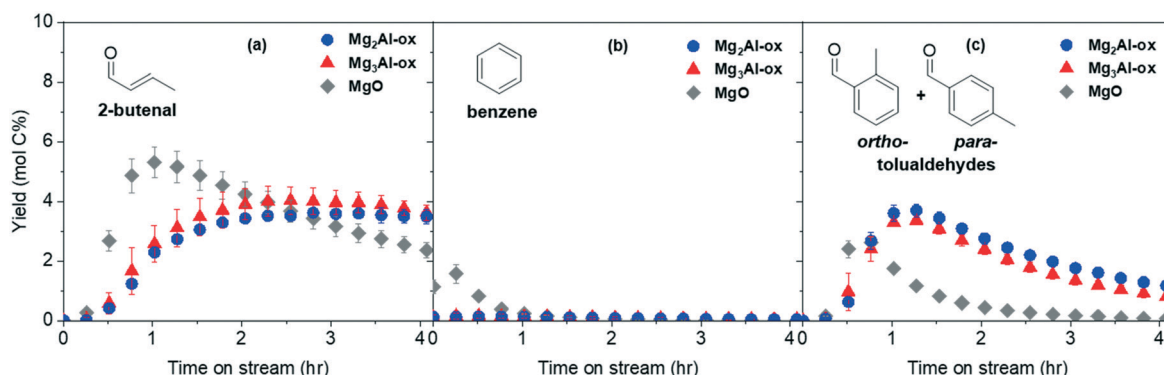
Fig. 4 Yields of products (a) 2-butenal, (b) benzene, and (c) tolualdehydes formed from acetaldehyde over Mg_xAl-ox and MgO catalysts (0.1% acetaldehyde/99.9% N_2, 10 sccm total flowrate, 10 mg catalyst, 250 °C, 1 bar).

2-Butenal forms through the self-aldol condensation of acetaldehyde. This mechanism is initiated by base deprotonation at the α-carbon (α-C) of acetaldehyde, generating an enolate intermediate. The enolate then executes a nucleophilic attack onto the carbonyl-C of the second acetaldehyde, forming the C_4 aldol which dehydrates to 2-butenal.[63–65] Previous studies of the vapor phase aldol condensation of acetaldehyde have reported the active 2-butenal-forming site to be a medium-strength, M–O-type site.[19,23,65,66]

Tolualdehydes (*ortho*- and *para*-) can form through 2 main routes.[12] The first route involves a cascade reaction: acetaldehyde self-condenses to its dimer, 2-butenal. Next, acetaldehyde undergoes a cross-condensation with 2-butenal to form the linear trimer, 2,4-hexadienal. Finally, acetaldehyde undergoes a second cross-condensation with the trimer to form the linear tetramer, 2,4,6-octatrienal (route 1, $C_2 + C_6$). The second route (route 2, $C_4 + C_4$) occurs *via* a bimolecular reaction between two molecules of the acetaldehyde dimer, 2-butenal. These routes form C_8 intermediates, which can undergo further reaction (deprotonation, electrocyclization, *etc.*) to form tolualdehydes. We did not detect the formation of any linear (2,4-hexadienal, 2,4,6-octatrienal) enals, which is not surprising given the unstable nature of polyenals, particularly at high temperatures ($T_{reaction}$ = 250 °C).[11,67]

Yields of tolualdehyde reach a maximum at time on stream (TOS) ≤ 1.25 h over all catalysts prior to decaying (Fig. 4c). Regardless of which routes are contributing ($C_2 + C_6$, $C_4 + C_4$), 2-butenal is an intermediate in tolualdehydes formation. Over the Mg_xAl-ox catalysts, the 2-butenal and tolualdehyde yields are comparable regardless of Al content. If the availability of the intermediate (2-butenal) is the same for these catalysts (given by comparable 2-butenal yields and similar desorption quantities after flushing the reactor at high temperature), this suggests that the density of the active basic site(s) is approximately constant over these materials. The tolualdehyde-formation activity loss over time could be due to acetaldehyde and 2-butenal consumption in other pathways and/or site deactivation. We observe a decrease in

side product formation (*e.g.*, ethyl acetate) from acetaldehyde after 1 h on stream and detect no other major products that consume 2-butenal (<1 mol% of the total carbon). This indicates deactivation of the tolualdehyde-forming site(s) is the primary cause of the decrease in tolualdehyde yields over time. Deactivation is consistent with the decay in acetaldehyde conversion over all samples (Fig. S8†), the color change of the spent catalysts to brown from white (*e.g.*, spent MgO in Fig. S8 inset†), and the weight loss between 400 and 500 °C in the TGA profiles of the spent samples that is absent in those of the fresh samples (not shown). The active site for 2-butenal is also likely deactivating, albeit slowly, because we do not measure a commensurate increase in the intermediate (2-butenal, Fig. 4a) yields as the consumption in tolualdehyde pathways decreases.

MgO exhibits similar trends for both 2-butenal and tolualdehydes, except that activity occurs at earlier TOS and decays more quickly. The strong basic character of pure MgO contributes to extensive formation of multiple condensation products that are nonvolatile at reaction conditions, particularly at early TOS prior to deactivating.[15,26,30] Even if the active basic site(s) are similar over MgO and Mg_xAl-ox, the deactivation mechanisms available over purely basic MgO differ from those over acid–base bifunctional Mg_xAl-ox, creating disparate profiles over time.[68]

Mg_xAl-ox and MgO show tolualdehyde formation activity that does not directly correlate with the total basic site density (Table 1). This suggests that, assuming comparable availabilities of relevant intermediates (*e.g.*, similar yield profiles for 2-butenal at 1.5 < TOS < 3.5 h, and no significant surface coverages evidenced by post-reaction flushes) not all basic site types contribute to the formation of tolualdehydes. Within each main tolualdehyde-forming route, there are subroutes that differ based on the position of the enolate (nucleophile) and the site of the nucleophilic attack (electrophile). The relative contributions of these subroutes dictate the observed selectivity towards each isomer (*ortho*- or *para*-). The isomeric selectivity is constant throughout TOS (section 3.4), despite the concurrent activity loss for tolualdehydes production. This strongly suggests that there is

This journal is © The Royal Society of Chemistry 2020

Catal. Sci. Technol., 2020, **10**, 536–548 | **541**

one dominant basic site and corresponding subroutes (*i.e.*, subroutes initiated by the same basic site deprotonation) responsible for the formation of these isomers; otherwise, we would expect to see a change in the isomeric selectivity as deactivation occurs.[11,69] It is possible that multiple basic sites and subroutes initiated by distinct deprotonation steps are contributing and exhibit identical rates of deactivation, but this is less likely.

3.3 Nature of the active basic site for toluladehyde formation from intermediates

3.3.1 *In situ* CO_2 titration. To begin identifying the nature of the active basic site, we conducted *in situ* titration of strong basic sites with CO_2.[23] In these experiments, activity from low-coordinated O^{2-} sites is selectively eliminated due to poisoning by CO_2—these strong sites bind CO_2 at temperatures greater than the reaction temperature of 250 °C, leaving only weak and medium-strength basic sites available for the reaction. Fig. 5a and b report the activity of the CO_2-titrated catalysts for production of 2-butenal and toluladehydes, respectively. The full product distributions measured over the *in situ* CO_2 titrated catalysts are shown in Fig. S11.†

The toluladehyde yields are maintained for all four catalysts, indicating that strong sites are not responsible for toluladehydes (or 2-butenal) production over Al-substituted or pure MgOs at these reaction conditions. The slight increase in toluladehyde yields over CO_2-titrated Mg_xAl-ox can be attributed to the fact that, upon selective deactivation of strong sites, relatively more acetaldehyde and intermediates are available to interact with the medium-strength or weak basic site responsible for toluladehydes production. Over CO_2-titrated MgO, the maximum yield of toluladehydes is greater (4.8 mol C%) and also occurs at earlier TOS (0.25 h) compared to the untreated sample (2.4 mol C%, 0.5 h). This can also be attributed to the elimination of activity from strong sites, which consume acetaldehyde and/or intermediates in nonvolatile product-forming routes at early TOS prior to deactivating.[30] Similarly, because early TOS activity is not dominated by strong sites, yields of 2-butenal are also detected earlier (0.25 h, rather than 0.5 h) over CO_2-titrated MgO. Since 2-butenal is an intermediate

involved in the production of toluladehyde, the increased production of 2-butenal likely contributes to improved toluladehyde formation kinetics. Despite the slight increases in toluladehyde yields over all catalysts, the profile shapes (after the initial activity shift over MgO) are essentially unchanged across untreated and CO_2-titrated samples, which shows that strong, low-coordinated O^{2-} basic sites present in MgO-based catalysts do not participate significantly in the toluladehydes formation mechanism.

3.3.2 Spent catalyst CO_2 DRIFTS. We conducted CO_2 DRIFTS studies on spent MgO to further probe the nature of the toluladehydes-forming basic site. As discussed earlier, the active site deactivates, and it does so irreversibly: activity is not regained after flushing the surface with N_2 at 450 °C and reintroducing acetaldehyde. Thus, it is no longer available to adsorb CO_2, an acidic probe molecule, and the carbonate structure attributed to the deactivated site will not manifest in the DRIFTS spectra on the spent catalyst. In this analysis, we neglect spectral differences for mono-/poly-dentate modes (*i.e.*, from strong O^{2-} basic sites) because these sites were shown by the *in situ* CO_2 titration experiments to be inactive for toluladehydes production. CO_2 DRIFTS measurements on spent MgO after 5 hours on stream (to reach near complete deactivation, toluladehydes yield <0.001 mol C%) are reported in Fig. 6a and b. The full temperature range is reported in Fig. S12a.† This analysis is strictly limited to a qualitative comparison between spectra at different temperatures.

All three carbonate structures (bicarbonate, bidentate, and monodentate-type) are present on the fresh MgO sample at 100 °C. The spectrum for the spent sample at this
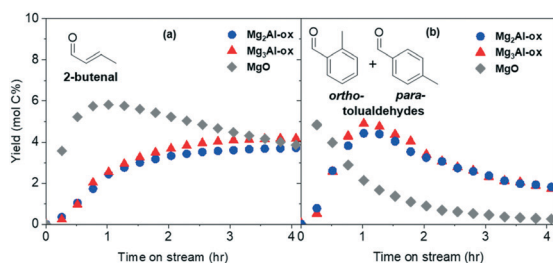
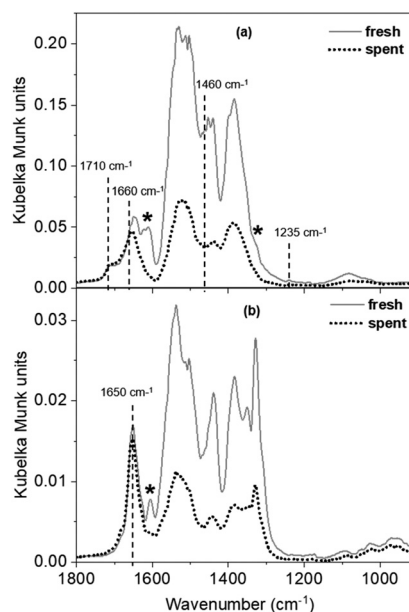**Fig. 6** CO_2 DRIFTS spectra over fresh and spent MgO at (a) 100 °C and (b) 200 °C. Frequency values marked with dashed lines indicate the features that are present in both spectra for the fresh and spent samples. Asterisks (*) denote the carbonate modes that are absent in the spent MgO spectra due to deactivation of the sites that give rise to these modes.

Fig. 5 Yields of products (a) 2-butenal and (b) toluladehydes formed from acetaldehyde over *in situ* CO_2-titrated Mg_xAl-ox and MgO catalysts (0.1% acetaldehyde/10% CO_2/89.9% N_2, 10 sccm total flowrate, 10 mg catalyst, 250 °C, 1 bar).

542 | *Catal. Sci. Technol.*, 2020, **10**, 536–548

This journal is © The Royal Society of Chemistry 2020

temperature (Fig. 6a) shows retainment of bicarbonate features corresponding to the distinct modes at 1710 and 1660 cm^{-1} (asymmetric), and those with relatively weaker intensities at 1460 cm^{-1} (symmetric) and 1235 cm^{-1} (bending; Fig. S12b† shows the y axis decreased to 0.02 Kubelka Munk units to see this small feature more clearly). Weakly basic hydroxyl groups, which are responsible for the formation of bicarbonate structures on MgO catalysts, are still available for CO_2 uptake on the spent sample. Because no substantial activity is observed (<0.001 mol C% tolualdehydes) despite the availability of the intermediate (2-butenal) and the weak basic sites to adsorb CO_2, these sites are not the tolualdehydes-forming active basic site. These results, in conjunction with the analysis from the strong site titration experiments, leave the remaining active site candidate to be a medium-strength, M–O-type site. The absence of bidentate carbonate structures that arise from CO_2 adsorption on these M–O-type sites at ~1610 cm^{-1} and ~1325 cm^{-1} ($v(C{=}O)$ and asymmetric $v(O–C–O)$, respectively, denoted by asterisks in Fig. 6a) supports this result. The loss of these carbonate structures is consistent with the loss of tolualdehyde activity, both due to site deactivation.

Many M–O-type surface coordination environments can give rise to medium-strength (between 120 and 150 kJ mol^{-1}) basic centers, depending on the oxygen site's nearest neighbors (≤5 bonds with M^{n+}, where M^{n+} is Mg^{2+} for pure MgO, and Mg^{2+} or Al^{3+} for Mg_xAl-ox) and proximity to defects (*e.g.*, edges, vacancies). However, not all medium-strength sites deactivated after 5 h on stream, which suggests that a site in specific M–O coordination is responsible for the formation of tolualdehydes over these materials. This is apparent in the CO_2 DRIFTS spectra at 200 °C (Fig. 6b), where the loss of bicarbonate structures due to increased temperature facilitates visualization of different bidentate $v(C{=}O)$ modes (1600–1650 cm^{-1}) that likely correspond to CO_2 adsorbed on distinctly-coordinated M–O-type sites.[70] Features at lower frequencies are more difficult to differentiate because of the strong intensities of monodentate/polydentate modes that persist at this temperature. The M–O-type site that gives rise to the mode at 1605 cm^{-1} deactivates, as this feature is absent in the spent spectrum (Fig. 6b, denoted by an asterisk), in contrast to the site that produces the persistent peak at 1650 cm^{-1}. This suggests that this former (lower frequency $v(C{=}O)$ mode) site is the active site for tolualdehydes formation. At this point, the exact coordination environment of this M–O site, and whether it is a unique site from that which is active for 2-butenal production, remain unclear.

The breadth of the CO_2 DRIFTS spectra for Mg_xAl-ox caused by the wider distribution of basic sites on these relatively more disordered structures makes distinguishing specific features more difficult. However, we expect the active basic site that initiates the formation of tolualdehyde through deprotonation to be in the same coordination sphere in Mg_xAl-ox (M–O-type) as in MgO because they are all the same phase (periclase). The small spinel domains do not appear to contribute to tolualdehyde activity since the tolualdehyde yields do not scale with spinel content (Fig. S2† and 4c). Similar to pure MgO, the active site is specifically-coordinated; otherwise, Mg_xAl-ox with different densities of different medium-strength sites (Fig. 2, CO_2 TPD profile for Mg_2Al-ox compared to that for Mg_3Al-ox at $200 < T < 450$ °C) would give rise to dissimilar yields of tolualdehydes for comparable 2-butenal and side product activity. Yet, these yields are very similar for both Al-substituted samples (Fig. 4a and c).

3.4 Tolualdehydes formation pathways and isomeric selectivity

The isomeric fraction (defined by the molar ratio of *ortho-* to total (*ortho-* + *para-*) tolualdehydes produced) is plotted in Fig. 7. The regions corresponding to the first 0.5 h on stream over all catalysts and at ≥3 h over MgO are not quantitatively reliable because the yields are so low (see Fig. 4c). An ASPEN simulation (Table S1†) determined that the equilibrium distribution of *ortho-* and *para*-tolualdehydes favors *para-* by over a factor of 2 (Fig. 7). Given that the *ortho*-isomeric fraction is >0.5 over all catalysts in the present study, *ortho*-tolualdehyde is the kinetic product. At TOS > 0.5 h, a constant isomeric fraction of 0.81 and 0.92 is measured over Mg_xAl-ox and MgO, respectively.

Within route 1 (C_2: acetaldehyde + C_6: 2,4-hexadienal), we considered six different subroutes including the most probable enolates, electrophiles, and dehydration positions involved in an aldol-type condensation based on a natural bond orbital (NBO) charge distribution analysis (Table 2). Computational details for the NBO charge density analysis are contained in the ESI† (Tables S2–S4†). The C_2 α-enolate can add to the C_6-carbonyl, -β, and -δ carbons; and the C_6 α-, γ-, and ε- enolates can add to the C_2-carbonyl carbon (Scheme S3†). Of these subroutes, only three yield C_8 enals capable of electrocyclization to tolualdehydes: 1A, 1B, and 1C. Routes 1A, $1B^2$, and 1C all yield *ortho*-tolualdehyde, while $1B^1$ produces *para*-tolualdehyde. $1B^1$ and $1B^2$ both involve the C_6 α-enolate
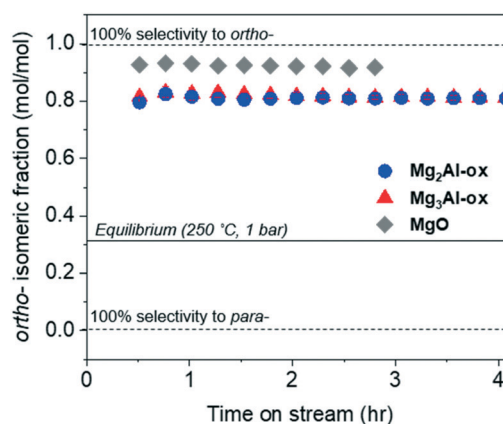

Fig. 7 The *ortho*-tolualdehyde isomeric fraction measured over TOS for Mg_xAl-ox and MgO catalysts.

This journal is © The Royal Society of Chemistry 2020

Catal. Sci. Technol., 2020, **10**, 536–548 | 543

Table 2 NBO charge distributions at carbon positions in acetaldehyde, 2-butenal, and 2,4-hexadienal

Carbon position	Acetaldehyde (C_2)	2-butenal (C_4)	2,4-hexadienal (C_6)
Carbonyl	0.438	0.391	0.381
α	−0.683	−0.309	−0.288
β	—	−0.087	−0.131
γ	—	−0.618	−0.247
δ	—	—	−0.104
ε	—	—	−0.613

adding to the C_2 carbonyl-C, but the formation mechanism of the enolate is different. In $1B^1$, the C_6 α-enolate is formed by direct deprotonation of the sp^2 α-C, while in $1B^2$, it forms as a resonance structure from deprotonation at the sp^3 ε-C. Direct deprotonation at the sp^2 α-C is considerably less favorable, given the inability to undergo π-delocalization of the negative charge, unlike for the ε-C deprotonation, which results in a highly conjugated anion.[71,72]

In the route 1 mechanisms outlined in Scheme S3,† no single deprotonation step initiates the formation of both *ortho-* and *para*-tolualdehyde; the formation of both isomers, which we experimentally observe, would require C_6-ε or C_2-α *and* C_6-α deprotonation. Given the active basic site and deactivation analysis that suggests a single site and deprotonation step are responsible for the formation of both isomers, in addition to the high kinetic cost of deprotonation of an sp^2 carbon (C_6-α), it is improbable that route 1 ($C_2 + C_6$) is occurring to any significant extent in the formation of tolualdehydes over these Mg_xAl-ox and MgO catalysts. This is further supported by the fact that benzene activity is very low over these materials (Fig. 4b, <0.5 mol C% over Mg_xAl-ox, 2 mol C% at TOS < 1 h before decay to <0.5 mol C% over MgO). At this reaction temperature (250 °C), cyclodehydration of the C_6 linear trimer (2,4-hexadienal) to benzene is likely more facile than the aldol condensation ($C_2 + C_6$).[14,67] Thus, if route 1 mechanisms were contributing significantly to tolualdehydes production, we would expect greater benzene activity over these catalysts.

Within route 2 (C_4: 2-butenal + C_4: 2-butenal), C_4 enolates (α- and γ-) can add to C_4 electrophiles (carbonyl- and β-carbons), giving rise to 4 subroutes, 2A–2D.[12] In this analysis, we consider only the C_4 α-enolate formed as the resonance structure achieved by deprotonation at the C_4 γ-C (sp^3), not the C_4 α-enolate that could theoretically form by direct C_4 α-C (sp^2) deprotonation (Fig. S13†). While we discuss these two enolates (C_4 α- and γ-) as distinct intermediates to differentiate the positions of the nucleophilic attack, it is a single intermediate with a delocalized charge. Scheme 2 summarizes the four subroutes initiated by base deprotonation of the C_4 γ-C. Routes 2A, $2C^2$, and 2D result in *ortho*-tolualdehyde, while 2B and $2C^1$ form the *para-* isomer.

Previous kinetic studies[12] of 2-butenal and 2-butenal surrogates (2-butenol, 3-methyl-2-butenal) over hydroxyapatite
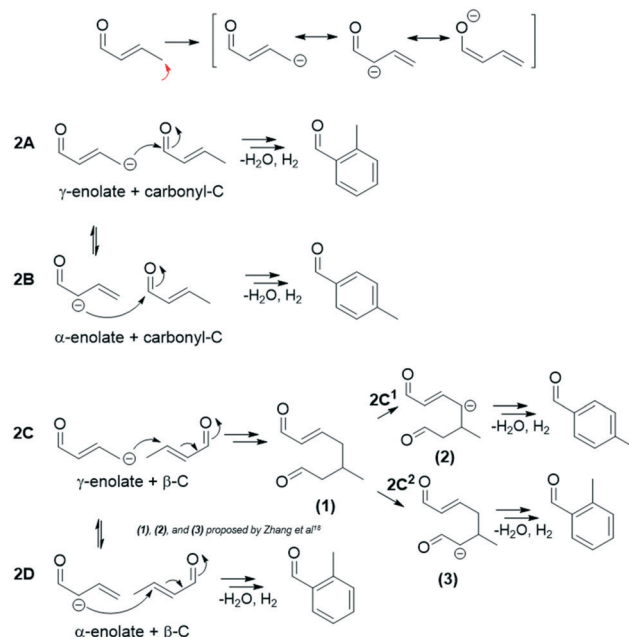
Scheme 2 The four subroutes of route 2 (C_4: 2-butenal + C_4: 2-butenal) initiated by γ-C deprotonation that yield tolualdehydes.[12,18]

catalysts at similar temperatures investigated here revealed that routes 2A and 2B dominate tolualdehydes production. We postulate that routes 2A and 2B are primarily responsible for the yields of *ortho-* and *para*-tolualdehydes, respectively, in this work as well, given that the carbonyl-C position is significantly more electrophilic (0.391) than the β-C (−0.087), and that routes 2C and 2D require additional deprotonation steps.[12,18] While we cannot conclusively rule out routes 2C and 2D, these factors make them less kinetically favorable *a priori*. In-depth mechanistic understanding through a complete DFT study of intermediate and transition state barriers for these complex pathways would facilitate further understanding of feasible tolualdehyde formation routes.

We measure a significantly higher selectivity towards the *ortho-* isomer (>80 mol C%) across all catalysts (Fig. 7). Wang and co-workers[17] measured similar isomeric selectivity (~85 mol C%) over Co-hydroxyapatite catalysts at 325 °C and a factor of 10 larger acetaldehyde concentration (diluted in N_2) than the concentration investigated here. Steric and electronic effects could be contributing to this, among other factors (*e.g.*, transition state stability).[73] Sterically, attack from the terminal γ-C might be less hindered than that from the mid-chain α-C, which would favor higher *ortho-* selectivity. Electronic considerations involve the negative charge delocalization throughout the C_4–O chain due to conjugation after the γ-C is deprotonated by the base site.[71,72] The NBO charge distribution calculation of the γ-deprotonated enolate intermediate (Table S5†) shows that the electronegative oxygen atom in the carbonyl group bears the most negative charge (−0.749); yet the γ-C still has a large negative charge density (−0.607), more so than the α-C (−0.474). The excess negative charge in the enolate intermediate is more

544 | *Catal. Sci. Technol.*, 2020, **10**, 536–548

This journal is © The Royal Society of Chemistry 2020

concentrated at the γ-C position compared to the α-C, which might suggest that the γ-enolate is a more represented nucleophile compared to the α-enolate. The higher density of the γ-C nucleophile would result in more contributions by route 2A (γ-enolate + carbonyl-C) compared to 2B (α-enolate + carbonyl-C), giving rise to a high *ortho-* selectivity as measured over these catalysts.

3.5 Role of catalyst acidity

3.5.1 Effect of Lewis acidity on isomeric selectivity. While the tolualdehyde formation mechanisms over the MgO-based catalysts studied here are initiated by the abstraction of a proton from the γ-C of 2-butenal by a basic site, the decrease in the *ortho-* isomeric fraction (Fig. 7) for Mg_xAl-ox (0.81) compared to pure MgO (0.92) highlights the impact of acidity on the tolualdehyde-forming routes. To rule out particle size effects since periclase derived from LDH precursors (*i.e.*, Al^{3+}/MgO) can have smaller particle sizes[74] compared to pure MgO, we ran a nanosized MgO sample (~300 nm particles, Sigma-Aldrich). The isomeric selectivity was 0.93 for this sample, similar to that for the MgO sample prepared by co-precipitation. This suggests that Al^{3+} incorporation, rather than particle size differences (and the associated effects on basic properties), are responsible for the isomeric selectivity shift. Lewis acid centers like those generated by Al^{3+} substitution in MgO are known to act as adsorption sites for electron-donating carbonyl oxygens.[66,75,76] Previous studies[30,34–38] have reported that acid sites can facilitate the nucleophilic attack (*e.g.*, in an aldol mechanism) by increasing the electrophilicity of the carbonyl-C bonded to a carbonyl-O adsorbed on an acid site. However, activation of the carbonyl-C of the neutral 2-butenal *via* the Al^{3+}–carbonyl-O interaction would not likely impact the isomeric selectivity in routes 2A and 2B, since increased electrophilicity of the carbonyl-C would not necessarily favor one route over the other (they have the same electrophile). We propose a different role of the acid sites in routes 2A and 2B. Al^{3+} cations in Mg_xAl-ox act as Lewis acid adsorption centers for

the carbonyl-O of the γ-deprotonated C_4 enolate intermediate, which redistributes the negative charge throughout the conjugated molecule (Fig. 8).

As an electron acceptor, the Lewis acid site draws the negative charge and stabilizes the enolate intermediate, which is feasible because the conjugation of the molecule is preserved.[77] We hypothesize that this electron flow towards the carbonyl-O coordinated to the Lewis acid shifts the negative charge density in the carbon chain originally localized on the γ-C towards the α-C, thereby making the α-enolate a more represented nucleophile. This allows route 2B to contribute more appreciably. As a result, we detect a selectivity shift towards *para*-tolualdehyde for Al-substituted MgO. The isomeric selectivity is not increasingly affected by an increased density of Lewis acid Al^{3+} sites in Mg_xAl-ox with increasing Al content (Table 1), even for a sample with Mg/Al = 1 and an even higher acid site density (1.74 µmol m^{-2}; not shown). This indicates two primary findings. First, the charge redistribution by Al^{3+}/carbonyl-O reduces the *ortho-* selectivity to a minimum value of 81%. This could be due to reduced, but still large, negative charge density on the γ-C, as well as other persistent steric or transition state stability effects that are not surmounted by the presence of more Lewis acidic Al^{3+} sites. Second, the density of acid centers needed to impact isomeric selectivity appears to far exceed that of the density of enolates formed by base deprotonation of the γ-carbon of 2-butenal. Even for the lower Al content of the Mg_xAl-ox (Mg/Al = 3), Al^{3+} effects on the enolate stability are saturated; otherwise, we expect the isomeric selectivity to be measured as a weighted fraction given by the relative amounts of sites with and without Al^{3+} effects and this value would change as Al content increases from 25 to 33 mol%.

3.5.2 Requirements for proximal Lewis acid centers. To investigate the importance of acid center proximity to the active basic site in the MgO catalysts, we repeated the acetaldehyde condensation on a mechanical (macroscopically biphasic) mixture of MgO and γ-Al_2O_3 with molar Mg/Al = 2. γ-Al_2O_3 exhibits high acid character due to coordinatively-unsaturated surface Al^{3+} and moderate-to-low basicity.[39,40] The XRD patterns for these samples and the yields of 2-butenal and tolualdehydes are reported in Fig. S14 and S15,† respectively. The *ortho-* isomeric fraction (Fig. S16†) for the mechanical mixture experiment is intermediate between that of the pure phases (MgO and γ-Al_2O_3). At early TOS, this value for the mechanical mixture (0.89) is closer to that for pure MgO (0.92) than for γ-Al_2O_3 (0.83). Over time, the *ortho-* fraction steadily drops to 0.85. These results show that the MgO dominates at early TOS, which is expected given its strong basic character.[30,68] As the MgO deactivates, the tolualdehyde yields are increasingly attributed to γ-Al_2O_3 activity, which is why the *ortho-* fraction for the mixture decays towards that of the pure γ-Al_2O_3 sample. In the biphasic mechanical mixture, the catalysts contribute as weighted representatives of the pure phases; the isomeric selectivity over MgO catalysts is only impacted by Lewis acid centers arising from isomorphic Al^{3+} substitution in
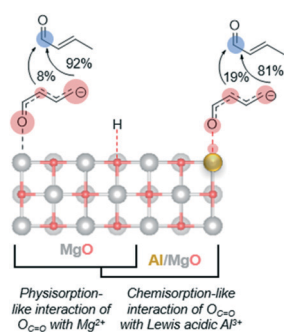

Fig. 8 A schematic of the proposed negative charge distribution (indicated by the size of red bubbles) in the conjugated C_4 enolate over the {100} surface of pure MgO (minimal acidity) and Mg_xAl-ox (Lewis acidity *via* Al^{3+}). Red and blue denote electron-rich and electron-poor atoms, respectively. Mg: silver, O: red, Al: gold.

This journal is © The Royal Society of Chemistry 2020

Catal. Sci. Technol., 2020, **10**, 536–548 | **545**

periclase. The enolate intermediate formed by deprotonation by a M–O-type basic site on MgO will apparently react with the second 2-butenal molecule *via* a nucleophilic attack on a timescale shorter than that for diffusion to another domain (*i.e.*, the γ-Al_2O_3 phase). Thus, proximal acid-active base sites, with Al^{3+} centers located nearby the active M–O coordinate sphere, are required to impact the effective density of the α-enolate and selectivity to *para*-tolualdehyde.

Conclusions

In this work, we investigated the impact of MgO catalyst surface chemistry on the formation of valuable aromatic platform chemicals from acetaldehyde, an ethanol derivative. In particular, we studied the nature of the active basic site for the formation of tolualdehydes, the isomers of which are oxidized intermediates in the synthesis of high-volume chemicals (phthalic anhydride, terephthalic acid) from xylenes. Through selective poisoning of strong basic sites, we showed that low-coordinated O^{2-} sites do not measurably contribute to the formation of tolualdehydes. This, in conjunction with the CO_2 DRIFTS experiments, identifies the active basic site over MgO-based catalysts to be a medium-strength site in a specific M–O coordination environment. The wide distribution of sites obtained on samples synthesized through the co-precipitation technique, coupled with the inherent disorder (*e.g.*, spinel nuclei) of calcined LDHs, make elucidating the precise coordination environment of this active site difficult on these catalysts. Yet, the finding that the active coordination sphere is M–O-type enables targeted syntheses of materials with well-defined M–O surface environments for continued investigation of potential catalysts.

While tolualdehydes can be produced from the cross-condensation of acetaldehyde with its linear trimer aldol product, 2,4-hexadienal (route 1, C_2 + C_6), the high likelihood of a single active basic site initiating the formation of both isomers, the large kinetic costs of sp^2-C deprotonation, and the minimal benzene yields rule out significant contributions from this pathway. *Ortho*- and *para*-tolualdehydes are more probably forming through the condensation of the acetaldehyde self-condensation product, 2-butenal (route 2, C_4 + C_4), *via* nucleophilic attack by the C_4 γ- and α-enolate, respectively, on the carbonyl-C of 2-butenal. We attribute the isomeric selectivity shift towards *para*- observed over the Mg$_x$-Al-ox to a charge distribution effect that occurs when the carbonyl-O of the enolate coordinates with a nearby Lewis acid Al^{3+} center: the negative charge in the intermediate is drawn to and stabilized by the electron acceptor, redistributing the charge density down the carbon chain from the initial locus of negative charge (γ-C) towards the acid site. This results in a higher charge density on the α-C than in the pure MgO case (minimal acid character), which increases the relative number of nucleophilic attacks occurring from the α-C to the carbonyl-C (route 2B) and shifts the isomeric selectivity towards *para*-. Even with this Lewis acid-mediated charge distribution effect that improves

para- selectivity, *ortho*-tolualdehyde remains the dominant product. Tailoring of the catalyst surface chemistry, along with other catalyst and reaction parameters, can be explored to further probe active site requirements for enhanced tolualdehyde yields and selectivity to the significantly more valuable *para*-isomer.

Conflicts of interest

There are no conflicts of interest to declare.

Acknowledgements

Notes and references

1 J. L. Pellegrino, *Energy and Environmental Profile of the U.S. Chemical Industry*, 2000.

2 B. Thompson, M. Machas and D. R. Nielsen, *Curr. Opin. Biotechnol.*, 2015, **36**, 1–7.

3 A. Maneffa, P. Priecel and J. A. Lopez-Sanchez, *ChemSusChem*, 2016, **9**, 2736–2748.

4 A. M. Niziolek, O. Onel, Y. A. Guzman and C. A. Floudas, *Energy Fuels*, 2016, **30**, 4970–4998.

5 P. C. A. Bruijnincx and B. M. Weckhuysen, *Angew. Chem., Int. Ed.*, 2013, **52**, 11980–11987.

6 C. L. Williams, K. P. Vinter, R. E. Patet, C. C. Chang, N. Nikbin, S. Feng, M. R. Wiatrowski, S. Caratzoulas, W. Fan, D. G. Vlachos and P. J. Dauenhauer, *ACS Catal.*, 2016, **6**, 2076–2088.

7 B. Dudley and S. Dale, *BP Statistical Review of World Energy*, 2017.

8 K. Cheng, W. Zhou, J. Kang, S. He, S. Shi, Q. Zhang, Y. Pan, W. Wen and Y. Wang, *Chem*, 2017, **3**, 334–347.

9 R. A. Sheldon, *J. Mol. Catal. A: Chem.*, 2016, **422**, 3–12.

10 T. Q. Hoang, X. Zhu, T. Sooknoi, D. E. Resasco and R. G. Mallinson, *J. Catal.*, 2010, **271**, 201–208.

11 T. Moteki, A. T. Rowley and D. W. Flaherty, *ACS Catal.*, 2016, **6**, 7278–7282.

12 T. Moteki, A. T. Rowley, D. T. Bregante and D. W. Flaherty, *ChemCatChem*, 2017, **9**, 1921–1929.

13 S. Hanukovich, A. Dang and P. Christopher, *ACS Catal.*, 2019, **9**, 3537–3550.

14 Y.-C. Chang and A.-N. Ko, *Appl. Catal., A*, 2000, **190**, 149–155.

15 H. Kurokawa, M. Yanai, M. A. Ohshima and H. Miura, *React. Kinet., Mech. Catal.*, 2012, **105**, 401–412.

16 T. Moteki and D. W. Flaherty, *ACS Catal.*, 2016, **6**, 4170–4183.

17 Q.-N. Wang, X.-F. Weng, B.-C. Zhou, S.-P. Lv, S. Miao, D. Zhang, Y. Han, S. L. Scott, F. Schüth, A.-H. Lu, P. F. Schüth and A.-H. Lu, *ACS Catal.*, 2019, **9**, 7204–7216.

18 L. Zhang, T. N. Pham, J. Faria, D. Santhanaraj, T. Sooknoi, Q. Tan, Z. Zhao and D. E. Resasco, *ChemSusChem*, 2016, **9**, 736–748.

19 J. I. Di Cosimo, V. K. Díez, M. Xu, E. Iglesia and C. R. Apesteguía, *J. Catal.*, 1998, **178**, 499–510.

20 C. Angelici, M. E. Z. Velthoen, B. M. Weckhuysen and P. C. a. Bruijnincx, *Catal. Sci. Technol.*, 2015, **5**, 2869–2879.

21 S. Ordóñez, E. Díaz, M. León and L. Faba, *Catal. Today*, 2011, **167**, 71–76.

22 M. León, E. Díaz and S. Ordóñez, *Catal. Today*, 2011, **164**, 436–442.

23 C. R. Ho, S. Shylesh and A. T. Bell, *ACS Catal.*, 2016, **6**, 939–948.

24 Q.-N. Wang, B.-C. Zhou, X.-F. Weng, S.-P. Lv, F. Schüth and A.-H. Lu, *Chem. Commun.*, 2019, **1**, 2–5.

25 S. Luo and J. L. Falconer, *J. Catal.*, 1999, **185**, 393–407.

26 E. Garrone, D. Bartalini, S. Coluccia, G. Martra, D. Tichit and F. Figueras, *Stud. Surf. Sci. Catal.*, 1994, **90**, 183–193.

27 Y. Tang, G. Chen and Y. Lu, *Res. Chem. Intermed.*, 2012, **38**, 937–946.

28 H. Idriss and M. A. Barteau, *Catal. Lett.*, 1996, **40**, 147–153.

29 H. Idriss, C. Diagne, J. P. Hindermann, A. Kiennemann and M. A. Barteau, *J. Catal.*, 1995, **155**, 219–237.

30 V. V. Ordomsky, V. L. Sushkevich and I. I. Ivanova, *J. Mol. Catal. A: Chem.*, 2010, **333**, 85–93.

31 J. Quesada, L. Faba, E. Díaz, S. Bennici, A. Auroux and S. Ordóñez, *J. Catal.*, 2015, **329**, 1–9.

32 G. S. Salvapati, K. V. Ramanamurty and M. Janardanarao, *J. Mol. Catal.*, 1989, **54**, 9–30.

33 J. I. Di Cosimo, V. K. Díez, C. Ferretti and C. R. Apesteguía, *Catalysis*, 2014, **26**, 1–28.

34 R. W. Snell, E. Combs and B. H. Shanks, *Top. Catal.*, 2010, **53**, 1248–1253.

35 M. J. Climent, A. Corma, S. Iborra and A. Velty, *J. Mol. Catal. A: Chem.*, 2002, **182–183**, 327–342.

36 G. D. Yadav and P. Aduri, *J. Mol. Catal. A: Chem.*, 2012, **355**, 142–154.

37 J. Tai and R. J. Davis, *Catal. Today*, 2007, **123**, 42–49.

38 E. Dumitriu, V. Hulea, C. Chelaru, C. Catrinescu, D. Tichit and R. Durand, *Appl. Catal., A*, 1999, **178**, 145–157.

39 J. Shen, J. M. Kobe, Y. Chen and J. A. Dumesic, *Langmuir*, 1994, **10**, 3902–3908.

40 J. Shen, M. Tu and C. Hu, *J. Solid State Chem.*, 1998, **137**, 295–301.

41 P. Kustrowski, L. Chmielarz, E. Boz, P. Kus, M. Sawalha and F. Roessner, *Mater. Res. Bull.*, 2004, **39**, 263–281.

42 I. M. Hill, S. Hanspal, Z. D. Young and R. J. Davis, *J. Phys. Chem. C*, 2015, **119**, 9186–9197.

43 J. Sirita, S. Phanichphant and F. C. Meunier, *Anal. Chem.*, 2007, **79**, 3912–3918.

44 M. J. Frisch, G. W. Trucks, H. B. Schlegel, G. E. Scuseria, M. A. Robb, J. R. Cheeseman, G. Scalmani, V. Barone, G. A.

Petersson, H. Nakatsuji, X. Li, M. Caricato, A. V. Marenich, J. Bloino, B. G. Janesko, R. Gomperts, B. Mennucci, H. P. Hratchian, J. V. Ortiz, A. F. Izmaylov, J. L. Sonnenberg, D. Williams-Young, F. Ding, F. Lipparini, F. Egidi, J. Goings, B. Peng, A. Petrone, T. Henderson, D. Ranasinghe, V. G. Zakrzewski, J. Gao, N. Rega, G. Zheng, W. Liang, M. Hada, M. Ehara, K. Toyota, R. Fukuda, J. Hasegawa, M. Ishida, T. Nakajima, Y. Honda, O. Kitao, H. Nakai, T. Vreven, K. Throssell, J. A. Montgomery Jr., J. E. Peralta, F. Ogliaro, M. J. Bearpark, J. J. Heyd, E. N. Brothers, K. N. Kudin, V. N. Staroverov, T. A. Keith, R. Kobayashi, J. Normand, K. Raghavachari, A. P. Rendell, J. C. Burant, S. S. Iyengar, J. Tomasi, M. Cossi, J. M. Millam, M. Klene, C. Adamo, R. Cammi, J. W. Ochterski, R. L. Martin, K. Morokuma, O. Farkas, J. B. Foresman and D. J. Fox, *Gaussian 16, Revision C.01*, Gaussian, Inc., Wallingford CT, 2016.

45 E. D. Glendening, A. E. Reed, J. E. Carpenter and F. Weinhold, *NBO Version 3.1*.

46 S. H. Vosko, L. Wilk and M. Nusair, *Can. J. Phys.*, 1980, **58**, 1200–1211.

47 D. O. Scanlon, A. Walsh, B. J. Morgan, M. Nolan, J. Fearon and G. W. Watson, *J. Phys. Chem. C*, 2007, **111**, 7971–7979.

48 S. V. Cherepanova, N. N. Leont'eva, A. B. Arbuzov, V. a. Drozdov, O. B. Belskaya and N. V. Antonicheva, *J. Solid State Chem.*, 2015, **225**, 417–426.

49 R. D. Shannon, *Acta Crystallogr.*, 1976, **32**, 751–767.

50 T. Sato, K. Kato, T. Endo and M. Shimada, *React. Solids*, 1986, **2**, 253–260.

51 J. Zhang, W. Qian, C. Kong and F. Wei, *ACS Catal.*, 2015, **5**, 2982–2988.

52 D. Meloni, R. Monaci, V. Solinas, A. Auroux and E. Dumitriu, *Appl. Catal., A*, 2008, **350**, 86–95.

53 J. A. Lercher, *React. Kinet. Catal. Lett.*, 1982, **20**, 409–413.

54 T. Armaroli, T. Bécue and S. Gautier, *Oil Gas Sci. Technol.*, 2004, **59**, 215–237.

55 M. A. Aramendia, V. Borau, C. Jimenez, J. M. Marinas, A. Porras and F. J. Urbano, *J. Mater. Chem.*, 1996, **6**, 1943–1949.

56 F. Prinetto, G. Ghiotti, V. P. Giuria, R. Durand and D. Tichit, *J. Phys. Chem. B*, 2000, **104**, 11117–11126.

57 J. A. Lercher, C. Colombier and H. Noller, *J. Chem. Soc., Faraday Trans.*, 1984, **80**, 949–959.

58 J. C. Lavalley, *Catal. Today*, 1996, **27**, 377–401.

59 A. Travert, A. Vimont, A. Sahibed-Dine, M. Daturi and J. C. Lavalley, *Appl. Catal., A*, 2006, **307**, 98–107.

60 F. Prinetto, G. Ghiotti, P. Graffin and D. Tichit, *Microporous Mesoporous Mater.*, 2000, **39**, 229–247.

61 G. Busca and V. Lorenzelli, *Mater. Chem.*, 1982, **7**, 89–126.

62 G. N. Vayssilov, M. Mihaylov, P. S. Petkov, K. I. Hadjiivanov and K. M. Neyman, *J. Phys. Chem. C*, 2011, **115**, 23435–23454.

63 M. Singh, N. Zhou, D. K. Paul and K. J. Klabunde, *J. Catal.*, 2008, **260**, 371–379.

64 D. Fan, X. Dong, Y. Yu and M. Zhang, *Phys. Chem. Chem. Phys.*, 2017, **19**, 25671–25682.

65 H. Zhang, M. Y. S. Ibrahim and D. W. Flaherty, *J. Catal.*, 2018, **361**, 290–302.

This journal is © The Royal Society of Chemistry 2020

Catal. Sci. Technol., 2020, **10**, 536–548 | **547**

66 B. I. Stefanov, Z. Topalian, C. G. Granqvist and L. Österlund, *J. Mol. Catal. A: Chem.*, 2014, **381**, 77–88.

67 M. Ros and E. J. J. Groenen, *J. Chem. Phys.*, 1991, **94**, 7640–7648.

68 V. K. Díez, C. R. Apesteguía and J. I. Di Cosimo, *Lat. Am. Appl. Res.*, 2003, **33**, 79–86.

69 J. E. Rekoske and M. A. Barteau, *Ind. Eng. Chem. Res.*, 2011, **50**, 41–51.

70 G. Martra, *Appl. Catal., A*, 2000, **200**, 275–285.

71 J. E. Bartmess and J. P. Kiplinger, *J. Org. Chem.*, 1986, **51**, 2173–2176.

72 I. Iriarte, O. Olaizola, S. Vera, I. Gamboa, M. Oiarbide and C. Palomo, *Angew. Chem., Int. Ed.*, 2017, **56**, 8860–8864.

73 E. M. P. Silva and A. M. S. Silva, *Synthesis*, 2012, **44**, 3109–3128.

74 M. del Arco, C. Martin, I. Martin, V. Rives and R. Trujillano, *Spectrochim. Acta, Part A*, 1993, **49**, 1575–1582.

75 Y. Roman-Leshkov and M. E. Davis, *ACS Catal.*, 2011, **1**, 1566–1580.

76 J. D. Lewis, S. Van de Vyver and Y. Roman-Leshkov, *Angew. Chem., Int. Ed.*, 2015, **54**, 9835–9838.

77 S. Herrmann and E. Iglesia, *J. Catal.*, 2017, **346**, 134–153.

548 | *Catal. Sci. Technol.*, 2020, **10**, 536–548

This journal is © The Royal Society of Chemistry 2020